Faraday Discussions

Cite this: *Faraday Discuss.*, 2017, **197**, 207

PAPER

Carbon induced selective regulation of cobalt-based Fischer–Tropsch catalysts by ethylene treatment†

Peng Zhai,‡[a] Pei-Pei Chen,‡[bc] Jinglin Xie,[a] Jin-Xun Liu,[b] Huabo Zhao,[a] Lili Lin,[a] Bo Zhao,[a] Hai-Yan Su,[b] Qingjun Zhu,[d] Wei-Xue Li*[bc] and Ding Ma*[a]

Received 19th September 2016, Accepted 10th October 2016
DOI: 10.1039/c6fd00194g

Various carbonaceous species were controllably deposited on Co/Al_2O_3 catalysts using ethylene as carbon source during the activation process for Fischer–Tropsch synthesis (FTS). Atomic, polymeric and graphitic carbon were distinguished by Raman spectroscopy, thermoanalysis and temperature programmed hydrogenation. Significant changes occurred in both the catalytic activity and selectivity toward hydrocarbon products after ethylene treatment. The activity decreased along with an increase in CH_4 selectivity, at the expense of a remarkable decrease of heavy hydrocarbon production, resulting in enhanced selectivity for the gasoline fraction. *In situ* XPS experiments show the possible electron transfer from cobalt to carbon and the blockage of metallic cobalt sites, which is responsible for the deactivation of the catalyst. DFT calculations reveal that the activation barrier (E_a) of methane formation decreases by 0.61 eV on the carbon-absorbed Co(111) surface, whereas the E_a of the CH + CH coupling reaction changes unnoticeably. Hydrogenation of CH_x to methane becomes the preferable route among the elementary reactions on the Co(111) surface, leading to dramatic changes in the product distribution. Detailed coke-induced deactivation mechanisms of Co-based catalysts during FTS are discussed.

[a]*Beijing National Laboratory for Molecular Sciences, College of Chemistry and Molecular Engineering, Peking University, Beijing 100871, China. E-mail: dma@pku.edu.cn*

[b]*State Key Laboratory of Catalysis, Dalian Institute of Chemical Physics, Chinese Academic of Sciences, Dalian 116023, China*

[c]*College of Chemistry and Material Sciences, iChEM (Collaborative Innovation Center of Chemistry for Energy Materials), CAS Center for Excellence in Nanoscience, Hefei National Laboratory for Physical Sciences at the Micro-Scale, University of Science and Technology of China, Hefei, China. E-mail: wxli70@ustc.edu.cn*

[d]*National Institute of Clean-And-Low-Carbon Energy, Future Science & Technology City, Changping District, Beijing 102209, China*

† Electronic supplementary information (ESI) available. See DOI: 10.1039/c6fd00194g

‡ These authors contributed equally to this work.

Introduction

The catalytic performance of a catalyst is determined by the structure of the catalyst. Therefore, efforts have been made in the last few decades to investigate the control and modulation of size, composition, phase, morphology, as well as the exposed facets of the active catalytic material, and therefore to tune the activity and the selectivity of the catalyst.[1] The construction of a stable catalyst with a designated surface structure, or so-called catalytic-active surface ensembles, is the ultimate goal in catalyst design. Indeed, different approaches have been used for the control of the surface structure. For example, by using a 2nd metal, it is possible to modulate the surface pattern of metal or metal oxide catalysts. The added 2nd metal can form an intermetallic compound,[2] an alloy,[3] a core–shell structure,[4] or an island-/atomically decorated structure[5] with the main metal components, which can alter the surface structure as well as the electronic structure of the catalyst, leading to the demonstration of superior catalytic performance in specific reactions. Besides the use of a 2nd metal, the surface of metal or metal oxide catalysts could be modified by relatively soft materials including surfactants,[6] protection agents[7] as well as carbonaceous species[8] on the surface of the catalyst. The carbonaceous species could be added during the preparation process of the catalyst, or be generated during the reaction process spontaneously. Normally, those carbonaceous species on the metal surface were treated as inactive species that block the active sites of the metal catalysts. However, it has been realized recently that they may have a major impact on the catalytic performance as well.[9] In this paper, we will use the carbon on a Co catalyst as an example to demonstrate the effect of this previously neglected species in heterogeneous catalysis.

Fischer–Tropsch synthesis is a catalytic process that transforms syngas, derived from coal, natural gas or biomass, to a wide spectrum of hydrocarbons involving diesel, gasoline and lower olefins. The design of efficient catalysts to produce desired products is one of the most important research topics. In contrast to the bulk iron-based catalysts used in industry, supported cobalt catalysts remain competitive because of their higher activity and selectivity towards long-chain hydrocarbons at low temperature.[10] Particle size,[11,12] crystallographic structure[13] and the interactions between cobalt and supports or promoters[14,15] are directly related to the catalytic properties in FTS.[16] It is reported that when the cobalt particle size is smaller than 6–8 nm, the activity as well as the selectivity for methane increase with the increase in cobalt particle size.[17] Moreover, hexagonal close packed (hcp) Co shows higher intrinsic activity than face centred cubic (fcc) Co in most cases,[18] and it was revealed by a first-principles kinetic study that the former prefers a direct CO dissociation route whereas H-assisted CO dissociation is a more plausible route on the fcc Co surface.[19] Since the metallic cobalt is identified as the active site,[20,21] one effective strategy to design better Co catalysts is to vary the pretreatment conditions to change the initial physico-chemical state of cobalt species before the reaction to regulate the selectivity of FTS.[22]

Although cobalt has excellent properties in liquid fuel production at low temperature, the high cost of cobalt and noble metal promoters is of considerable burden to industry. Therefore, improving the stability of the catalyst is crucial to

ensure that the process is economically feasible. Various factors are recognized to cause a decrease in activity including particle sintering, the re-oxidation and carburization of cobalt, poisoning and carbon formation.[23,24] Carbon deposition occurs slowly in hydrogen-rich syngas, but it is a negligible problem under a hydrogen deficient atmosphere.[25] Both carbidic and polymeric carbon species were observed on Co/Al_2O_3 after extended runs; their accumulation blocked the active sites, resulting in a decrease in activity.[26] A long reaction time is required to observe a considerable amount of deposited carbon,[27] and the used catalysts are always contaminated by a large amount of heavy hydrocarbon products, which are difficult to be eliminated.[28] In order to investigate the role of carbon, some catalyst models have been established to simulate the process.[29,30] Weststrate *et al.* successfully constructed carbonaceous species on Co(0001), and found that the existence of atomic carbon weakens the adsorption of CO and H_2 on the cobalt surface and graphene completely blocks the active sites.[31] It has also been conjectured that the carbide reconstructed or graphene-covered Co(111) surface is the stable form during the reaction by density functional theory (DFT) calculations.[32] In contrast, carbon atoms are also suggested to induce the reconstruction of Co(0001), leading to the formation of step edge sites with low CO dissociation activation energy.[33] The correlations between carbonaceous species and catalytic performance in FTS are still under debate.

Ethylene is a favorable carbon source for graphene growth because of its low decomposition temperature.[34–36] It is interesting to note that cobalt is a feasible substrate for layered graphene deposition.[37] Carbon filament formation was observed on a reduced Co surface after being treated in a C_2H_4 and H_2 (1 : 1) atmosphere.[38] Therefore, ethylene was chosen to build up a deactivated Co/Al_2O_3 catalyst model in our research. In this report, we systematically investigated the detailed role of ethylene in the pre-treatment process, offering a new perspective for facilitating the reduction of cobalt. More importantly, coupled with various characterizations and DFT calculations, we attempt to reveal the deactivation mechanism of the cobalt catalyst in FTS.

Experimental

Preparation of Co/Al_2O_3 catalysts

The Co/Al_2O_3 catalysts were prepared by an impregnation method. Typically, 8.5 mmol of $Co(NO_3)_2 \cdot 6H_2O$ (AR) was dissolved in 20 mL ethanol, then the solution was added dropwise into 5 g γ-Al_2O_3 powder (high surface area, Alfa Aesar). After being stirred and dried at 60 °C, the mixture was calcined at 400 °C for 5 hours in a muffle furnace with a heating ramp of 2 °C min^{-1}. The obtained black powder was denoted as Co/Al. Prior to FTS, the catalysts were reduced by hydrogen or pretreated in 10% C_2H_4/H_2 at 450 °C for 3 hours. A number of Co/Al_2O_3 catalysts were prepared using various conditions (Table 1) to investigate the ethylene treatment effect on cobalt catalysts. Samples for *ex situ* characterizations were passivated by 1% O_2/N_2 at room temperature.

Catalytic tests

The Fischer–Tropsch reaction was carried out in a stainless continuous flow fixed-bed reactor with a 12 mm inner diameter quartz tube inside. 0.2 g Co/Al_2O_3

Table 1 Detailed synthesis conditions of the Co/Al_2O_3 catalysts

Sample	Reduction condition	Treatment
Co–H	H_2	
Co–H–C1	H_2	C_2H_4 250 °C/1 h
Co–H–C3	H_2	C_2H_4 250 °C/3 h
Co–M	10% C_2H_4/H_2	
Co–M–H	10% C_2H_4/H_2	H_2 450 °C/3 h

catalyst sieved into 40–60 mesh was diluted with 1 g inert SiC. Prior to the catalytic test, the catalyst was *in situ* pretreated at atmospheric pressure with a gas flow rate of 20 mL min^{-1}. The pretreated conditions were identical to those used in the catalyst preparation. After cooling down below 100 °C, the system was switched to 3.0 MPa syngas with the composition of $H_2/CO/Ar = 64/32/4$ (molar ratio). The reaction was operated at 230 °C with a weight hourly space velocity (WHSV) of 6000 mL $g_{cat.}^{-1}$ h^{-1}.

The gas products were analyzed on-line by an Agilent 7890A GC. CO, H_2, CH_4, CO_2 and C_2H_6 were analyzed using a thermal conductivity detector (TCD) and the other gas products were analyzed through an alumina capillary column with a hydrogen flame ionization detector (FID). Liquid products including oxygenates collected from a cold trap were analyzed off-line by an Agilent 7820A GC. The selectivity of solid wax products was determined by weight. All the selectivity was determined on a carbon basis.

Characterization and computation method

Inductively coupled plasma atomic emission spectrometry (ICP) was performed to determine the cobalt content. X-ray diffraction (XRD) and transmission electron microscopy (TEM) were used to observe the morphology of cobalt. Thermogravimetry and differential scanning calorimetry (TG/DSC) and Raman spectroscopy were employed to analyze the carbonaceous species. Detailed information about the characterization is referred to in the ESI.†

The X-ray absorption spectroscopy spectra (XAFS) were acquired on a beamline BL14W1-XAFS at Shanghai Synchrotron Radiation Facility (SSRF). The storage ring was operated at 3.5 GeV and 300 mA using a Si(111) double-crystal monochromator. XAFS signals were measured in transmission mode at the Co absorption K-edge. Co_3O_4 powder grounded with hexagonal boron nitride was used as the reference material.

Temperature programmed hydrogenation (TPH) experiments were carried out in a quartz tube fixed bed micro-reactor. 50 mg of sample was hydrogenated in 5% H_2/N_2 (50 mL min^{-1}) ranging from 50 °C to 800 °C with a ramp rate of 10 °C min^{-1}. A Pfeiffer GSD320 mass spectrometer was used to monitor the CH_4 fragments as a function of temperature.

The X-ray photoelectron spectroscopy (XPS) measurements were conducted on an Axis Ultra Imaging Photoelectron Spectrometer equipped with an Al Kα (1486.7 eV) quartz monochrometer source. The sample wafers were pre-treated inside a treatment chamber with the reaction gas (H_2, C_2H_4 or 10% C_2H_4/H_2). The treatment conditions were identical to the conditions for the catalyst

preparation. The chamber was connected to the vacuum system; thus the samples were transferred to the measurement chamber by a slide without exposure to air.

Periodic spin-polarized density functional theory (DFT) calculations were conducted to study the CO activation, methanation and C_{2+} formation on pure and carbon-decorated Co(111) surfaces (denoted as Co and C/Co surfaces). The top two Co layers and adsorbates were allowed to fully relax and the bottom two metal layers were fixed. The calculated lattice constant of bulk Co with a face-centered cubic structure is $a = b = c = 3.52$ Å, which is consistent with the experimental value of 3.55 Å.[39] Detailed information about the calculations is referred to in the ESI.†

Results and discussion

Structure characterization of cobalt

The XRD patterns of calcined Co/Al_2O_3 catalysts are displayed in Fig. 1. All of the diffraction peaks of Co/Al are indexed to the Co_3O_4 phase except for the γ-Al_2O_3 peaks. The crystallite size of Co_3O_4 is estimated by the Scherrer equation ($D = K\lambda/B \cos\theta$) to be 11.8 nm. Nevertheless, Co–H exhibits peaks at 2θ values of 44.22° and 51.52°, which correspond to fcc Co (JCPDS # 15-0806), after the reduction in pure H_2. In addition, a peak at a 2θ value of 42.40° assigned to CoO (JCPDS # 43-1004) is also observed, implying that Co_3O_4 is partially reduced under these conditions. Co–H–C1 and Co–H–C3 which are further treated with ethylene after reduction show similar patterns to Co–H. However, the characteristic peaks of metallic Co become more significant with the increase in ethylene treatment time, indicating that ethylene facilitates the reduction of cobalt oxide. Compared with Co–H, there is an apparent decrease of the metallic Co peak intensity on Co–M. Since no increase in CoO diffraction peak intensity is detected, the difference is attributed to the weakened degree of crystallinity of the cobalt particles.

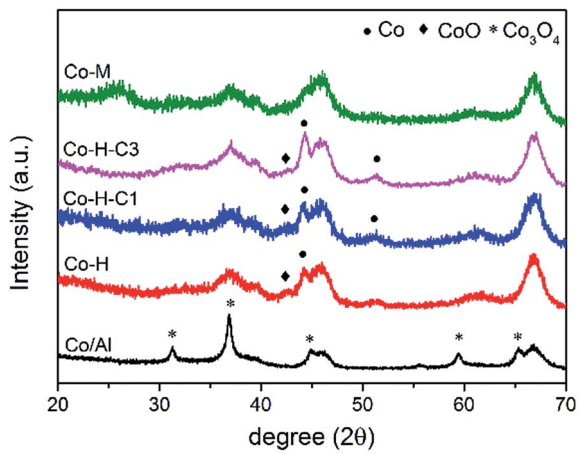

Fig. 1 XRD patterns of Co/Al_2O_3 catalysts.

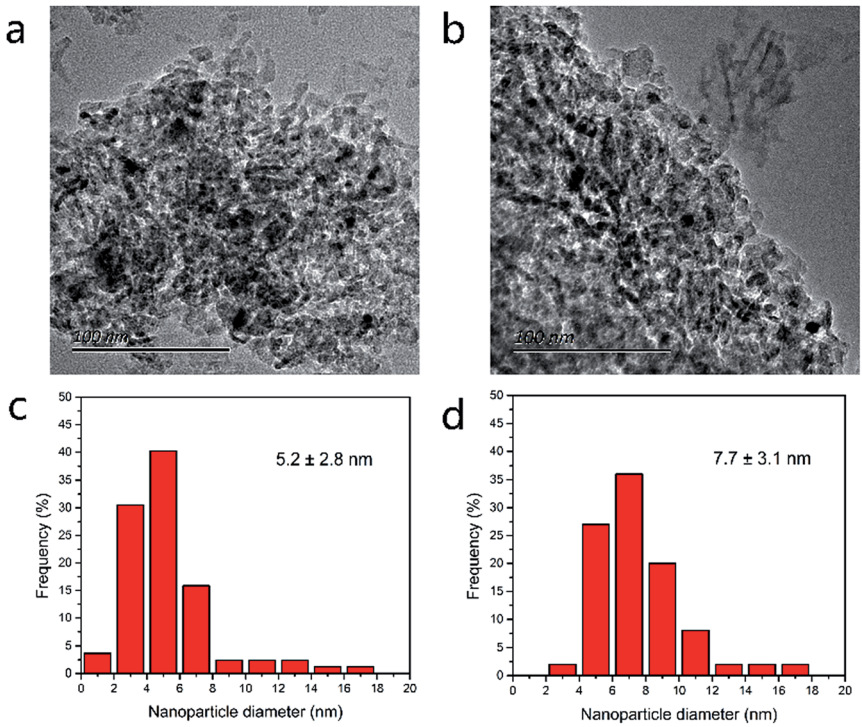

Fig. 2 TEM images and particle size distribution of Co/Al_2O_3 catalysts: (a and c) Co–H; (b and d) Co–M.

Fig. 2 presents TEM images of the Co/Al_2O_3 catalysts. It was found that Co/SiO_2 dried at 100 °C showed a smaller particle size and better aggregation-resisting properties compared to the catalyst dried at 175 °C,[40] and it was reported that ethoxyl groups that formed on the silica surface resulted in strong interactions between the cobalt and support.[41] In this work, the cobalt nitrate ethanol solution, instead of common aqueous solution, not only lowers the removal temperature of the solvent, but also hinders the sintering process of the precursor salt decomposition. Small and homogeneously dispersed cobalt nanoparticles are obtained consequently. In the case of Co–H, 85% of cobalt particles are in the range of 2–8 nm with an average diameter of 5.2 nm. Most of the particles are irregular spheres although several larger ones above 10 nm are also observed. When 10% C_2H_4/H_2 is used instead of pure H_2 during the pre-treatment process, the average particle size increases to 7.7 nm diameter. Moreover, the particle distribution becomes narrower and several pieces of graphitic carbon are identified in the micrographs.

The oxidation state of the cobalt species is investigated by XANES at the Co K-absorption edge (Fig. 3). In the spectra of the Co/Al_2O_3 catalysts, the entire peak shapes resemble the patterns between CoO and Co foils, indicating that the oxidation states of the three Co/Al_2O_3 catalysts are between Co(0) and Co(II), which is in accordance with the XRD patterns. The spectrum of Co–H is similar to the CoO reference, implying that this sample possesses the lowest reducibility of

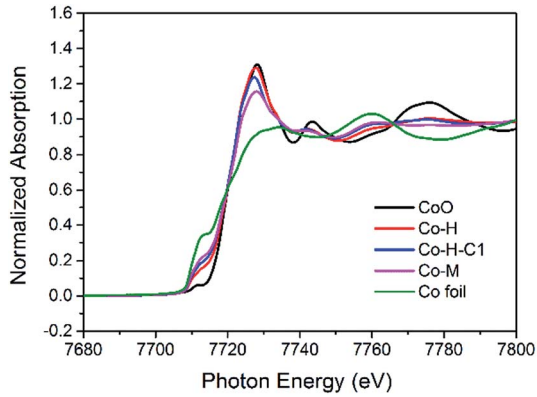

Fig. 3 Co K-edge XANES spectra of Co/Al_2O_3 catalysts.

cobalt out of all the catalysts. The degree of cobalt reduction, derived from the intensity of white lines at 7725 eV, shows a tendency as follows: Co–H < Co–H–C1 < Co–M. Table S1 and Fig. S1† exhibit the fitting results of the Fourier transform of the EXAFS data for the Co/Al_2O_3 catalysts. According to the coordination number of Co–Co which is a statistical average value for cobalt nanoparticles, Co–M has the largest cobalt particle size among the catalysts. The average diameter for Co–H is much smaller than for the samples treated by 10% C_2H_4/H_2, which is confirmed by TEM. Since the nucleation and growth of particles mainly occurs during calcination and reduction, the cobalt size of Co–H–C is similar to Co–H, which is verified by their similar Co–Co coordination numbers.

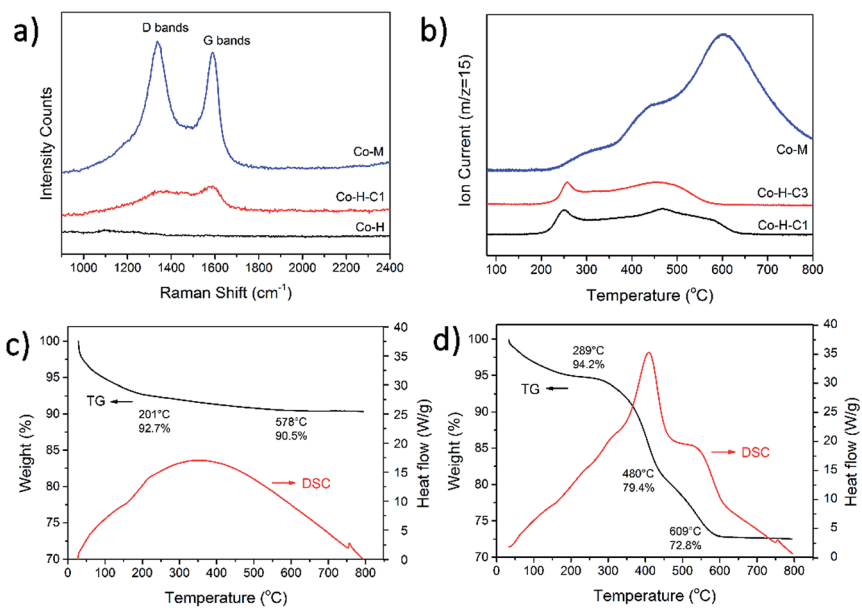

Fig. 4 Characterization of carbon on Co/Al_2O_3 catalysts: (a) Raman spectra, (b) TPH profiles, (c) TG and DSC behavior of Co–H–C1, (d) TG and DSC behavior of Co–M.

Characterization of carbon on catalysts

The Raman spectra of Co/Al_2O_3 catalysts are exhibited in Fig. 4a. No remarkable bands are visible for Co–H. Two relatively broad bands at about 1344 and 1591 cm^{-1}, which correspond to D (disordered) and G (graphitic) bands, are observed on Co–H–C1, pointing to the occurrence of carbon growth with poor crystallinity during the ethylene treatment. Moreover, the intensity of both the G-band and the D-band significantly increased on Co–M, indicating that the carbons are relatively well graphitized. TPH profiles are used to distinguish the different carbonaceous species because of their different reactivities toward H_2 (Fig. 4b).[26,42] The peak at 250 °C is assigned to the hydrogenation of atomic carbon species, indicating that carbide species may exist on the 250 °C ethylene carburized samples. Additionally, two broad peaks at around 450 °C and 600 °C on Co–M are ascribed to the hydrogenation of polymeric carbon and graphitic carbon species, respectively. It is generally recognized that the different positions of C 1s XPS peaks correspond to different forms of carbon species (Fig. S2†).[43,44] A slightly increased amount of carbon is observed on Co–H–C1, while the spectrum of Co–M shows typical characteristics of graphitic carbon.

The thermal behavior of the Co/Al_2O_3 catalysts was studied by TG-DSC measurements in an air atmosphere to elucidate the content and species of carbon (Fig. 4c and d). It is concluded that *ca.* 2.5% carbon is deposited (>200 °C) on Co–H–C1 during the carburization process. In comparison, the TG diagram presents two stages between 280 °C and 610 °C for Co–M, resulting in a 21.4% weight loss, which correspond to two forms of carbon. The first degradation stage with a 14% weight loss is assigned to the oxidation of amorphous carbon in the presence of cobalt, as evidenced by the heat release peak displayed on the DSC curve.[22] Pyrolysis of graphitic carbon seems to be a mild process in air, resulting in a second weight loss procedure above 450 °C.

Catalytic performance in Fischer–Tropsch synthesis

The Co/Al_2O_3 catalysts were investigated in FTS at 230 °C and 3.0 MPa (Fig. 5 and Table S2†); 28% CO conversion was achieved on Co–H at steady state. After being treated by C_2H_4, an obvious decrease in activity was observed on Co–H–C1 and

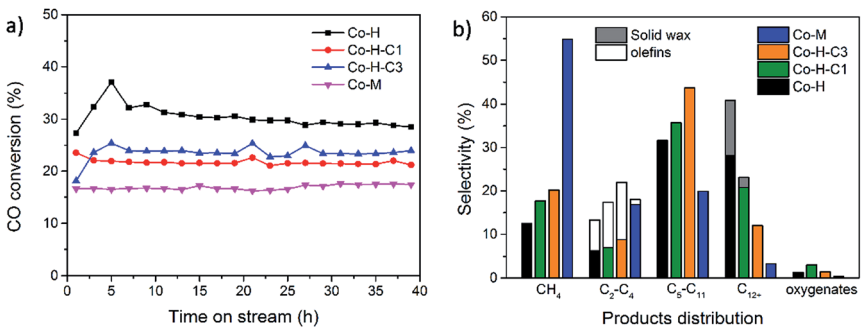

Fig. 5 The catalytic performance of Co/Al_2O_3 catalysts in FTS at 230 °C, 3.0 MPa, and a H_2/CO ratio of 2. (a) CO conversion as a function of time, (b) product distribution. The oxygenate component contains C1–C5 alcohols.

Co–H–C3. The lowest CO conversion (18% at steady state) was detected on Co–M, implying that there was a poisoning effect caused by the ethylene pre-reduction.

One of the notable characteristics that distinguish the catalysts is their different selectivities toward hydrocarbon products. As is shown in Fig. 5b, remarkable changes were observed after Co–H was treated with ethylene at 250 °C. The catalyst favored the formation of light fractions, and the tendency to form large molecular weight hydrocarbons was suppressed. The methane selectivity increased from 13% to 18% over the Co–H–C1 catalyst. Correspondingly, the selectivity in terms of C_{12+} products declined considerably from 41% to 23%. When the treatment time was prolonged to 3 hours, the production of hydrocarbons with a carbon number higher than 12 continuously decreased, the solid wax completely disappeared, and only 12% of diesel components remained. Interestingly, the gasoline fraction was enhanced from 31.6% to 43.7% on Co–H–C3 compared to Co–H, so the quality of the F–T products was improved by the ethylene treatment to some extent.

On the other hand, dramatic changes were observed on the 10% C_2H_4/H_2 treated sample. Co–M exhibited high selectivity toward methane (54.9%) and an extremely low C_{12+} production (3.3%). Furthermore, the production of olefins was almost completely inhibited which resulted in a significantly low olefin to paraffin (o/p) ratio (from 1.1 to 0.07). The enhanced CO_2 selectivity was related to the occurrence of the water–gas shift reaction (WGS, $CO + H_2O \rightarrow CO_2 + H_2$). It seems that the ethylene reduction atmosphere leads to a catalyst that prefers CH_4 formation, which is completely different from the diesel favoring catalyst. The continuously declining chain growing probability (α, from 0.82 to 0.71) clearly demonstrated that the chain growth ability was weakened by the ethylene treatment.

Discussion

We have investigated the influence of ethylene pre-treatment on the structure of the Co/Al_2O_3 catalysts, as well as the corresponding catalytic performance in FTS. The pure hydrogen reduced sample showed low methane selectivity and a strong capability of producing long-chain hydrocarbon products including solid wax. CO conversion decreased significantly and the CH_4 selectivity increased when ethylene participated in the activation process. The remarkable decrease of C_{12+} production indicates that the carbon chain propagation process is inhibited. A high o/p ratio is obtained on C_{5+} preferring catalysts, whereas a low olefin selectivity appears on the methane favoring catalyst. In general, the FTS performance of a cobalt-based catalyst depends on several factors: (1) the morphology and size of cobalt nanoparticles; (2) the phase of cobalt; (3) the degree of reduction; and (4) the surface state of the catalyst. Since CO hydrogenation is a structure-sensitive reaction, FTS performance is affected by the morphology and particle size of cobalt. It was reported that the FTS activity decreased with a decrease in the diameter of cobalt nanoparticles on carbon nanofibers, and CH_4 was the main product on particles smaller than 6 nm.[17,45] Our TEM images show that most of the cobalt particles are approximately irregular spheres between 5–10 nm in diameter. Although the particle diameter remained unchanged after being treated in ethylene at 250 °C, the CO conversion significantly declined. The small particles showed high selectivity toward C_{12+} products

while the larger ones produced a large amount of CH_4. It seems that the size effect is not the key factor in this system.

On the other hand, it has been confirmed that the crystal phase of cobalt plays a crucial role in the activity of the catalyst. Hcp Co reduced from cobalt carbide showed an enhanced FTS activity compared with fcc Co which is usually obtained in a reduced cobalt catalyst.[46] The carburization of cobalt oxide was always induced by CO at low temperature, and light hydrocarbons including ethylene were also believed to be effective carburizers.[47] Cobalt carbide is metastable under reducing atmospheres even at 220 °C,[46] and DFT calculations suggested it should have a higher methane selectivity than metallic Co.[48] However, no experimental evidence demonstrates that hcp Co is beneficial for CH_4 formation. Since it is difficult to discriminate between cubic and hexagonal phases of cobalt in XAFS,[49] and no clear diffraction fringe assigned to hcp Co domains is observed in HR-TEM and XRD, the change in catalytic selectivity is tentatively ascribed to other factors.

It is well known that it is difficult for Co_3O_4 to be completely reduced to the metallic phase without any other auxiliary metals such as Pt, Ru.[50,51] Because it is generally believed that metallic Co is responsible for the activity of the CO hydrogenation reaction, the Co metal concentration of cobalt species should be directly related to the catalytic activity. Both XRD and XAFS data offer information about the bulk structure of the particles; therefore, it is necessary to investigate the Co metal concentration on the surface where the FTS reaction occurs. Co 2p XPS spectra were collected *via* an *in situ* technique without exposure to air (Fig. 6). The noticeably low ratio of the surface to bulk cobalt suggests that the cobalt particles are preferentially located in alumina pores (Table S3†). It is also inferred that the majority of carbon is deposited on the catalyst surface, as is evidenced by the remarkably high ratio of surface to bulk carbon.

For Co–H, the intense peak at 777.6 eV is generally identified to be characteristic of metallic cobalt, and the broad shoulder at higher energy (~5 eV) suggests the existence of unreduced CoO.[52] A considerable amount of metallic Co exists on the surface, which is different from that in the bulk. Co–H–C1 shows a dramatic decrease in the intensity of the metallic Co peak after the carburation process. Combined with the 17% percentage increase of carbon on the C 1s spectra, carbon deposition is the most plausible reason for this phenomenon.

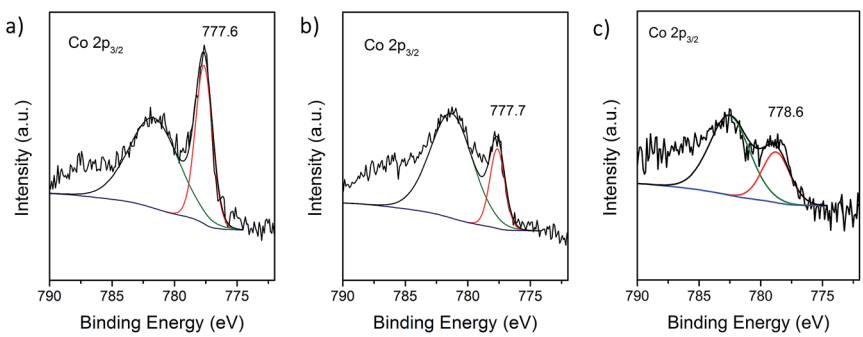

Fig. 6 Co $2p_{3/2}$ XPS spectra of Co/Al_2O_3 catalysts: (a) Co–H (b) Co–H–C1 (c) Co–M.

However, the relative peak of metallic Co in the Co–M spectrum shifts to 778.6 eV, indicating a change in the chemical environment of cobalt. The possible electron transfer from cobalt to graphitic carbon contributes to the apparent binding energy shift to high field.[53] In our previous work, we found that the electron-rich iron carbide prefers carbon chain growth and olefin production.[54] Correspondingly, the electron-deficient cobalt seems to facilitate the formation of low paraffin, and especially methane production in this work. Moreover, the remarkably weakened signal of Co–M spectrum demonstrates that the sample suffers severely from carbon deposition. As confirmed by Fig. 7, some cobalt nanoparticles in Co–M are surrounded by amorphous carbon with a low degree of graphitization, which decreases the cobalt concentration in the subsurface area. It is reported that carbon prefers to nucleate on step and defect sites of cobalt and then migrates to form large particles.[55] The growth of atomic carbon and carbon islands block partial active sites on Co–H–C, leading to a slight decrease in activity. When 10% C_2H_4/H_2 is used instead of H_2, the thicker graphitized carbon layers inhibit the reactant gas from coming into contact with the active sites, and thus a significantly decreased level of CO conversion is observed on Co–M.

To elucidate the influence of carbon on the selectivity of cobalt, we present a DFT study of methane formation and C–C coupling with or without pre-adsorbed carbon on fcc Co(111), which is observed in TEM and is suggested to be the most abundant facet exposed in many studies.[56–58] Since polymeric and graphitic carbons mainly cover and deactivate active sites,[59] atomically adsorbed carbons can be more relevant to tune the electronic structure of the substrate, which in turn change the relative activity of competing reaction pathways. Therefore, two models of pure and atomic carbon-decorated fcc Co(111)-(2 × 3) surfaces (denoted as Co and C/Co, respectively) are constructed. To simulate the carbon-decorated C/Co(111)-(2 × 3) surface, two atomic carbons (1/3 monolayer) were pre-adsorbed on the surfaces, as shown in Fig. 8.

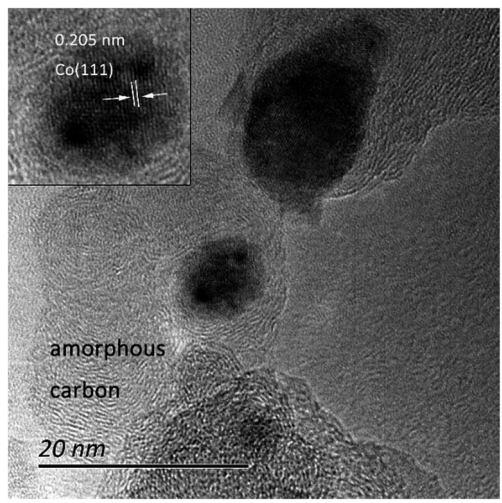

Fig. 7 HR-TEM picture of Co–M catalyst.

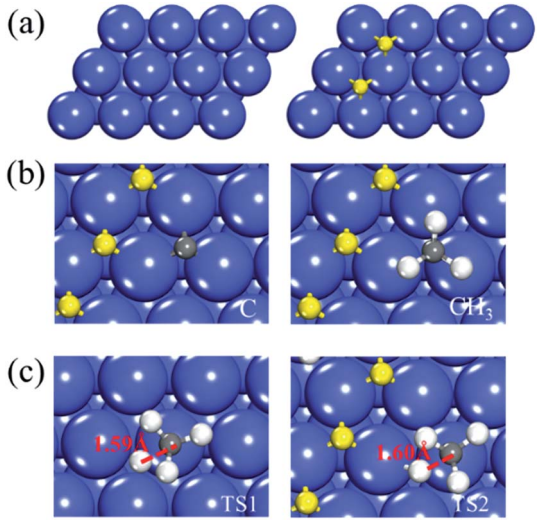

Fig. 8 (a) The schematic structures (top view) of Co(111) surfaces without (a) and with (b) atomic carbon in the $p(2 \times 3)$ unit cell. (b) Optimized structures of C and CH_3 species on C/Co surface (O has the same structure as C). (c) Transition states of CH_3 hydrogenation in Fig. 9. The blue and yellow balls represent Co and pre-adsorbed C atoms, respectively.

We first calculate the adsorption energies ΔE_{ads} of the reactive intermediates for methanation and C–C coupling on Co and C/Co, and the results are listed in Table S4.† In general, the C/Co surface binds the intermediates less strongly than the Co surface. C, O and CH_3 show the largest reduction in ΔE_{ads} by 0.46 eV, 0.59 eV and 0.52 eV, respectively, and the corresponding structures are shown in Fig. 8b. It can be seen that the intermediates share metal atoms with the pre-adsorbed C, leading to substrate-mediated repulsive interactions between adsorbates. In addition, CH_3 is tilted away from the pre-adsorbed C upon adsorption, which suggests that steric hindrance results in additional repulsion and a further decrease in ΔE_{ads}. The weakened intermediate binding not only facilitates the thermochemistry of methanation, as can be seen from the large reduction in the reaction heat ΔH by 1.03 eV for carbon hydrogenation, but also lowers the apparent activation energy by 0.61 eV, as seen in Fig. 9. These results indicate that the existence of carbon greatly accelerates methane formation on the cobalt surface, which is consistent with our experimental findings.

Various C–C couplings between CH_i ($i = 0$, 1, 2, and 3) were considered to study the effect of the pre-adsorbed C, and corresponding formation energies of intermediates E_i with respect to the most favorable CH were calculated. The formation energy ($E_i + E_j$) of intermediates between CH_i and CH_j and the corresponding activation barrier E_a for subsequent CH_i–CH_j couplings are listed in Table 2. The effective barriers (E_{eff}) are then achieved by the summation of E_a and $E_i + E_j$, which allows a direct comparison of the relative activity of the C–C coupling steps.[60] The E_a for the C–C coupling steps are generally lower on C/Co than on Co, which indicates that the weaker binding of intermediates with the pre-adsorbed C leads to more facile bond-forming reactions. When it comes to the effective barrier (E_{eff}), C*-involved couplings have a relatively high E_{eff} on both

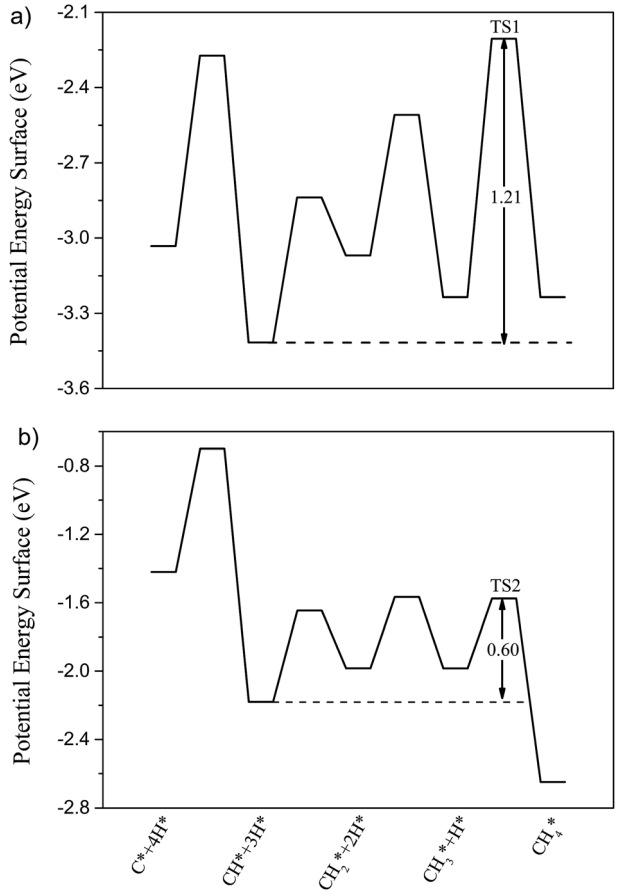

Fig. 9 The potential energy surfaces for CH_4 formation on Co (a) and C/Co (b), respectively. The apparent activation energies are denoted.

Table 2 The activation energies E_a, formation energies $E_i + E_j$ and E_{eff} for CH_i–CH_j ($i, j = 0$, 1, 2, 3) coupling on Co and C/Co

	Co			C/Co		
Reaction	E_a	$E_i + E_j$	E_{eff}	E_a	$E_i + E_j$	E_{eff}
C–C	1.09	0.76	1.85	0.87	1.52	2.40
C–CH	0.84	0.38	1.22	0.65	0.76	1.41
$C–CH_2$	0.73	0.73	1.46	0.47	0.96	1.43
$C–CH_3$	1.00	0.56	1.56	0.48	0.95	1.43
CH–CH	0.72	0.00	0.72	0.74	0.00	0.74
$CH–CH_2$	0.66	0.35	1.01	0.67	0.20	0.87
$CH–CH_3$	1.11	0.18	1.29	0.89	0.20	1.09
$CH_2–CH_2$	0.41	0.70	1.11	0.41	0.39	0.81
$CH_2–CH_3$	1.01	0.53	1.54	0.58	0.39	0.97

cobalt catalysts owing to their high formation energies, and thus this is less relevant for C–C coupling processes. However, for the remaining C–C coupling steps (Fig. S3†), the E_a and $E_i + E_j$ are basically lowered on C/Co, which dramatically decreases E_{eff}. Based on the E_{eff} calculations, the CH–CH coupling stands out with the lowest E_{eff} values of 0.72 and 0.74 eV on Co and C/Co, respectively. We have chosen this pathway as the most probable pathway for the C–C coupling process.

The comparison of the apparent barriers for methane formation and C–C coupling is shown in Fig. 10. Despite the similar apparent barriers of the C–C coupling process (0.72 eV *vs.* 0.74 eV), methane formation is more favorable on C/Co than on Co (0.60 *vs.* 1.21 eV), leading to greatly improved methane selectivity, which agrees well with our experimental studies.

The presence of carbonaceous species significantly changes the catalytic performance in FTS, leading to the deactivation of cobalt catalysts. To further investigate the regeneration properties of the cobalt catalyst under relevant conditions, Co–M was treated in H_2 at 450 °C for 3 hours to obtain Co–M–H. CO conversion on Co–M–H increased to 32% which was slightly higher than that on Co–H (Fig. 11). More importantly, the CH_4 selectivity decreased to 18% and the C_{12+} selectivity increased to 34%. A relative enhancement of the o/p ratio and inhibited WGS reactivity were also observed. It seems that the catalyst almost recovers the ability for chain growth and olefin desorption, which is very similar to Co–H. Although both the C 1s XPS spectrum and TG analysis demonstrated that only a small amount of carbon (11%) was eliminated during the hydrogenation treatment, metallic cobalt was exposed again on the surface of the catalyst, as revealed in the Co 2p XPS spectrum (Fig. S4†). Unlike the graphitic carbon deposited on Al_2O_3 which is resistant to hydrogen,[61] the carbon located on the cobalt is mostly eliminated, leading to recovered C–C coupling ability over Co–M–H. The carbon on Al_2O_3 is proposed to mainly act as a spectator during the FTS process (Fig. S6†).

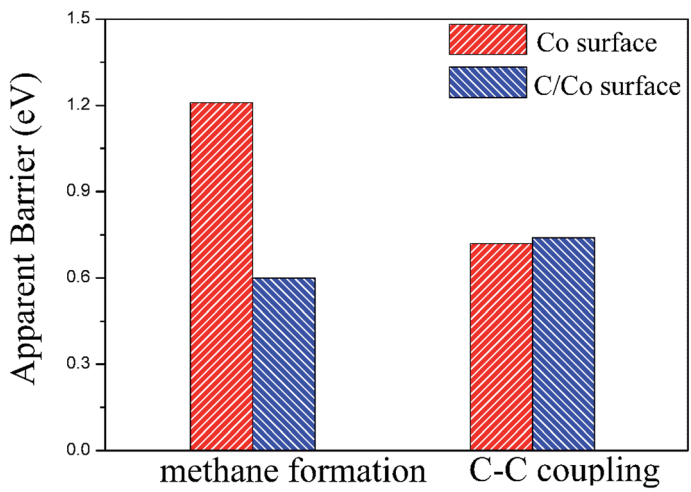

Fig. 10 Comparison of apparent barriers for methanation and C–C coupling. Red and blue columns represent Co and C/Co systems, respectively.

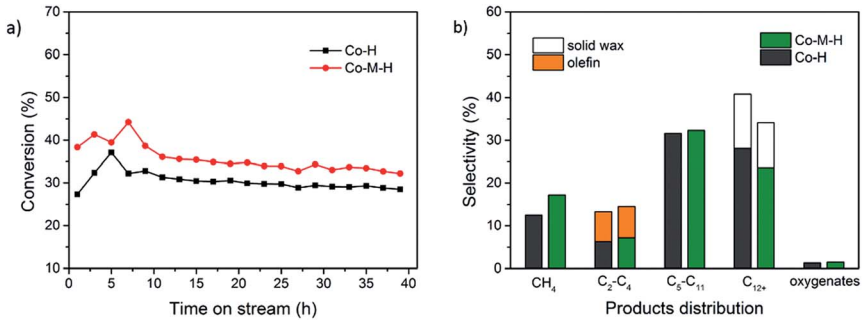

Fig. 11 Comparison of Co–M–H and CO–H catalytic performance in FTS at 230 °C, 3.0 MPa, and H_2/CO ratio of 2. (a) CO conversion as a function of time, (b) product distribution.

Conclusions

This report demonstrates that ethylene treatment has a remarkable influence on the structure of Co/Al_2O_3 catalysts through multiple aspects. Firstly, compared to the pure H_2 activated sample, the particle size tends to be larger in the 10% C_2H_4/H_2 treated sample. Secondly, although bulk cobalt carbide hardly exists under a hydrogen-rich environment, the possible carburization process contributes to enhance the reduction degree of cobalt. Finally, the different pretreatment conditions produce distinct carbon species on the surface of cobalt. Dispersed atomic carbon or polymeric carbons are generated at 250 °C in C_2H_4, and graphitic carbons are the predominant species on Co–M that are activated in 10% C_2H_4/H_2. Accordingly, the deposited carbons on the Co catalysts regulate the FTS selectivity by enhancing the low paraffin selectivity at the expense of decreasing C_{12+} production, especially the solid wax. The blockage of active sites either by atomic or graphitized carbon is responsible for the decreased catalyst activity. Nevertheless, the catalytic performance can be almost recovered by the hydrogenation of carbon atoms on cobalt sites at 450 °C. The treatment of ethylene is an efficient method to regulate the structure of cobalt nanoparticles for their catalytic activities in FTS and the coke deposition plays a dramatic role in terms of the product selectivity. Further DFT calculations suggest that carbon atoms on Co(111) not only increase the CO dissociation barrier but also change the activation energy of elementary reactions on the cobalt surface. Methane formation is preferred over C–C coupling on the carbon-adsorbed Co(111) surface, and the electron-deficient cobalt facilitates the hydrogenation of intermediates to produce low carbon number paraffins.

Statement of contribution

Ding Ma and Qingjun Zhu designed the study. Peng Zhai synthesized and evaluated the catalysts and participated in most of the characterization experiments and data analysis for the catalysts. Jinglin Xie did the in-situ XPS experiments. Huabo Zhao carried out the XAFS experiment. Lili Lin carried out the TEM observation and Bo Zhao did the TG analysis. Pei-Pei Chen did most of the DFT

calculations and Jin-Xun Liu constructed the model and discussed the results. Hai-Yan Su and Wei-Xue Li carried out analysis and discussed the DFT results.

Acknowledgements

This work was supported by the Natural Science Foundation of China (21473003, 21222306, 21473229, 91545121, 21273224, 21321002, 21225315), and the 973 Project of China (2013CB933100, 2013CB834603). We thank the SSRF for providing the beamline and Siyu Yao for data discussion.

Notes and references

1 K. Zhou and Y. Li, *Angew. Chem., Int. Ed.*, 2012, **51**, 602–613.
2 B. Y. Xia, H. B. Wu, X. Wang and X. W. Lou, *J. Am. Chem. Soc.*, 2012, **134**, 13934–13937.
3 F. Besenbacher, I. Chorkendorff, B. S. Clausen, B. Hammer, A. M. Molenbroek, J. K. Nørskov and I. Stensgaard, *Science*, 1998, **279**, 1913–1915.
4 M. B. Gawande, A. Goswami, T. Asefa, H. Guo, A. V. Biradar, D. L. Peng, R. Zboril and R. S. Varma, *Chem. Soc. Rev.*, 2015, **44**, 7540–7590.
5 B. Qiao, A. Wang, X. Yang, L. F. Allard, Z. Jiang, Y. Cui, J. Liu, J. Li and T. Zhang, *Nat. Chem.*, 2011, **3**, 634–641.
6 N. R. Jana, Z. L. Wang and T. Pal, *Langmuir*, 2000, **16**, 2457–2463.
7 M. I. Redondo and C. B. Breslin, *Corros. Sci.*, 2007, **49**, 1765–1776.
8 S. S. Chen, L. Brown, M. Levendorf, W. W. Cai, S. Y. Ju, J. Edgeworth, X. S. Li, C. W. Magnuson, A. Velamakanni, R. D. Piner, J. Y. Kang, J. Park and R. S. Ruoff, *ACS Nano*, 2011, **5**, 1321–1327.
9 C. Wang, P. Zhai, Z. C. Zhang, Y. Zhou, J. K. Zhang, H. Zhang, Z. J. Shi, R. P. S. Han, F. Q. Huang and D. Ma, *J. Catal.*, 2016, **334**, 42–51.
10 A. Y. Khodakov, W. Chu and P. Fongarland, *Chem. Rev.*, 2007, **107**, 1692–1744.
11 G. Prieto, A. Martinez, P. Concepcion and R. Moreno-Tost, *J. Catal.*, 2009, **266**, 129–144.
12 A. Tuxen, S. Carenco, M. Chintapali, C. H. Chuang, C. Escudero, E. Pach, P. Jiang, F. Borondics, B. Beberwyck, A. P. Alivisatos, G. Thornton, W. F. Pong, J. H. Guo, R. Perez, F. Besenbacher and M. Salmeron, *J. Am. Chem. Soc.*, 2013, **135**, 2273–2278.
13 D. I. Enache, B. Rebours, M. Roy-Auberger and R. Revel, *J. Catal.*, 2002, **205**, 346–353.
14 O. Borg, P. D. C. Dietzel, A. I. Spjelkavik, E. Z. Tveten, J. C. Walmsley, S. Diplas, S. Eri, A. Holmen and E. Ryttera, *J. Catal.*, 2008, **259**, 161–164.
15 H. Wang, W. Zhou, J. X. Liu, R. Si, G. Sun, M. Q. Zhong, H. Y. Su, H. B. Zhao, J. A. Rodriguez, S. J. Pennycook, J. C. Idrobo, W. X. Li, Y. Kou and D. Ma, *J. Am. Chem. Soc.*, 2013, **135**, 4149–4158.
16 P. Zhai, G. Sun, Q. J. Zhu and D. Ma, *Nanotechnol. Rev.*, 2013, **2**, 547–576.
17 G. L. Bezemer, J. H. Bitter, H. P. C. E. Kuipers, H. Oosterbeek, J. E. Holewijn, X. D. Xu, F. Kapteijn, A. J. van Dillen and K. P. de Jong, *J. Am. Chem. Soc.*, 2006, **128**, 3956–3964.
18 M. K. Gnanamani, G. Jacobs, W. D. Shafer and B. H. Davis, *Catal. Today*, 2013, **215**, 13–17.

19 J. X. Liu, H. Y. Su, D. P. Sun, B. Y. Zhang and W. X. Li, *J. Am. Chem. Soc.*, 2013, **135**, 16284–16287.
20 K. H. Cats, I. D. Gonzalez-Jimenez, Y. Liu, J. Nelson, D. van Campen, F. Meirer, A. M. van der Eerden, F. M. de Groot, J. C. Andrews and B. M. Weckhuysen, *Chem. Commun.*, 2013, **49**, 4622–4624.
21 N. E. Tsakoumis, R. Dehghan, R. E. Johnsen, A. Voronov, W. van Beek, J. C. Walmsley, Ø. Borg, E. Rytter, D. Chen, M. Rønning and A. Holmen, *Catal. Today*, 2013, **205**, 86–93.
22 L. Shi, Y. Z. Jin, C. Xing, C. Y. Zeng, T. Kawabata, K. Imai, K. Matsuda, Y. S. Tan and N. Tsubaki, *Appl. Catal., A*, 2012, **435**, 217–224.
23 N. E. Tsakoumis, M. Ronning, O. Borg, E. Rytter and A. Holmen, *Catal. Today*, 2010, **154**, 162–182.
24 A. M. Saib, D. J. Moodley, I. M. Ciobica, M. M. Hauman, B. H. Sigwebela, C. J. Weststrate, J. W. Niemantsverdriet and J. van de Loosdrecht, *Catal. Today*, 2010, **154**, 271–282.
25 P. G. Menon, *J. Mol. Catal.*, 1990, **59**, 207–220.
26 K. F. Tan, J. Xu, J. Chang, A. Borgna and M. Saeys, *J. Catal.*, 2010, **274**, 121–129.
27 D. J. Moodley, J. van de Loosdrecht, A. M. Saib, M. J. Overett, A. K. Datye and J. W. Niemantsverdriet, *Appl. Catal., A*, 2009, **354**, 102–110.
28 D. Pena, A. Griboval-Constant, V. Lecocq, F. Diehl and A. Y. Khodakov, *Catal. Today*, 2013, **215**, 43–51.
29 M. C. Zonnevylle, J. J. C. Geerlings and R. A. Vansanten, *Surf. Sci.*, 1990, **240**, 253–262.
30 J. C. W. Swart, E. van Steen, I. M. Ciobica and R. A. van Santenc, *Phys. Chem. Chem. Phys.*, 2009, **11**, 803–807.
31 C. J. Weststrate, A. C. Kizilkaya, E. T. R. Rossen, M. W. G. M. Verhoeven, I. M. Ciobica, A. M. Saib and J. W. Niemantsverdriet, *J. Phys. Chem. C*, 2012, **116**, 11575–11583.
32 M. C. Valero and P. Raybaud, *J. Phys. Chem. C*, 2014, **118**, 22479–22490.
33 X. Q. Zhang, R. A. van Santen and E. J. M. Hensen, *ACS Catal.*, 2015, **5**, 596–601.
34 H. Zhang, Q. Fu, Y. Cui, D. L. Tan and X. H. Bao, *J. Phys. Chem. C*, 2009, **113**, 8296–8301.
35 J. Lahiri, T. Miller, L. Adamska, I. I. Oleynik and M. Batzill, *Nano Lett.*, 2011, **11**, 518–522.
36 S. Gunther, S. Danhardt, M. Ehrensperger, P. Zeller, S. Schmitt and J. Wintterlin, *ACS Nano*, 2013, **7**, 154–164.
37 H. Ago, Y. Ito, N. Mizuta, K. Yoshida, B. Hu, C. M. Orofeo, M. Tsuji, K. Ikeda and S. Mizuno, *ACS Nano*, 2010, **4**, 7407–7414.
38 M. S. Kim, N. M. Rodriguez and R. T. K. Baker, *J. Catal.*, 1993, **143**, 449–463.
39 N. W. Ashcroft and N. D. Mermin, *Solid State Physics*, Holt, Rinehart and Winston, New York, 1976, p. 70.
40 P. Munnik, P. E. de Jongh and K. P. de Jong, *J. Am. Chem. Soc.*, 2014, **136**, 7333–7340.
41 S. W. Ho and Y. S. Su, *J. Catal.*, 1997, **168**, 51–59.
42 J. Xu and C. R. Bartholomew, *J. Phys. Chem. B*, 2005, **109**, 2392–2403.
43 J. M. Xiong, Y. J. Ding, T. Wang, L. Yan, W. M. Chen, H. J. Zhu and Y. Lu, *Catal. Lett.*, 2005, **102**, 265–269.
44 Y. J. Gao, D. Ma, G. Hu, P. Zhai, X. H. Bao, B. Zhu, B. S. Zhang and D. S. Su, *Angew. Chem., Int. Ed.*, 2011, **50**, 10236–10240.

45 J. P. den Breejen, P. B. Radstake, G. L. Bezemer, J. H. Bitter, V. Froseth, A. Holmen and K. P. de Jong, *J. Am. Chem. Soc.*, 2009, **131**, 7197–7203.
46 G. Kwak, M. H. Woo, S. C. Kang, H. G. Park, Y. J. Lee, K. W. Jun and K. S. Ha, *J. Catal.*, 2013, **307**, 27–36.
47 H. Karaca, O. V. Safonova, S. Chambrey, P. Fongarland, P. Roussel, A. Griboval-Constant, M. Lacroix and A. Y. Khodakov, *J. Catal.*, 2011, **277**, 14–26.
48 J. Cheng, P. Hu, P. Ellis, S. French, G. Kelly and C. M. Lok, *J. Phys. Chem. C*, 2010, **114**, 1085–1093.
49 J. C. Mohandas, M. K. Gnanamani, G. Jacobs, W. P. Ma, Y. Y. Ji, S. Khalid and B. H. Davis, *ACS Catal.*, 2011, **1**, 1581–1588.
50 N. Kumar, M. L. Smith and J. J. Spivey, *J. Catal.*, 2012, **289**, 218–226.
51 J. Y. Park, Y. J. Lee, P. R. Karandikar, K. W. Jun, J. W. Bae and K. S. Ha, *J. Mol. Catal. A: Chem.*, 2011, **344**, 153–160.
52 C. R. Brundle, T. J. Chuang and D. W. Rice, *Surf. Sci.*, 1976, **60**, 286–300.
53 J. Deng, P. J. Ren, D. H. Deng, L. Yu, F. Yang and X. H. Bao, *Energy Environ. Sci.*, 2014, **7**, 1919–1923.
54 P. Zhai, C. Xu, R. Gao, X. Liu, M. Li, W. Li, X. Fu, C. Jia, J. Xie, M. Zhao, X. Wang, Y. W. Li, Q. Zhang, X. D. Wen and D. Ma, *Angew. Chem., Int. Ed.*, 2016, **55**, 9902–9907.
55 H. S. Bengaard, J. K. Norskov, J. Sehested, B. S. Clausen, L. P. Nielsen, A. M. Molenbroek and J. R. Rostrup-Nielsen, *J. Catal.*, 2002, **209**, 365–384.
56 J. C. W. Swart, L. M. Ciobica, R. A. van Santen and E. van Steen, *J. Phys. Chem. C*, 2008, **112**, 12899–12904.
57 C. B. Chen, Q. Wang, G. R. Wang, B. Hou, L. T. Jia and D. B. Li, *J. Phys. Chem. C*, 2016, **120**, 9132–9147.
58 B. H. Li, Q. J. Zhang, L. A. Chen, P. Cui and X. Q. Pan, *Phys. Chem. Chem. Phys.*, 2010, **12**, 7848–7855.
59 C. Klink, I. Stensgaard, F. Besenbacher and E. Lagsgaard, *Surf. Sci.*, 1995, **342**, 250–260.
60 J. Cheng, P. Hu, P. Ellis, S. French, G. Kelly and C. M. Lok, *J. Phys. Chem. C*, 2009, **113**, 8858–8863.
61 I. Czekaj, F. Loviat, F. Raimondi, J. Wambach, S. Biollaz and A. Wokaun, *Appl. Catal., A*, 2007, **329**, 68–78.

